JTSES
Journal of Thermal and Sustainable Energy Systems
https://jtses.com/index.php/home/index

Multi-Nanoparticle Synergy in Ultra-High-Performance Concrete: Optimizing Strength, Durability, and Shrinkage Using RSM

M. Gowrisankar [1], Sudhagar Manickam [2], P. Rajasekar [3], Baskar Rathinam [4*]

[1] Department of Mechanical Engineering, Paavai College of Engineering, Namakkal – 637018, Tamil Nadu, India — Email: gsintamil@gmail.com

[2] Department of Mechatronics Engineering, Er. Perumal Manimekalai College of Engineering, Nallaganakothapalli, Hosur, Tamil Nadu, India — Email: sudhagar85@gmail.com

[3] Department of Mechanical Engineering, Paavai College of Engineering, Namakkal – 637018, Tamil Nadu, India — Email: rajasekarperumalpce@paavai.edu.in

[4] Department of Mechatronics Engineering, Mahendra Engineering College (Autonomous), Namakkal – 637503, Tamil Nadu, India — Email: baskarrathinam01@gmail.com

Corresponding Author*: Baskar Rathinam — Email: baskarrathinam01@gmail.com

Abstract

Ultra-High-Performance Concrete (UHPC) is emerging as a next-generation construction material due to its exceptional mechanical and durability properties. However, issues related to early-age shrinkage, limited workability, and cost-effective performance enhancement persist. To address these limitations, this study investigates the synergistic incorporation of nano-silica (NS), nano-alumina (NA), and carbon nanotubes (CNTs) into UHPC, a combination rarely explored in a unified optimization framework. The objective is to optimize these nanoparticles for enhanced compressive and flexural strength, reduced chloride permeability, and minimized shrinkage. A central composite design within a Response Surface Methodology (RSM) framework was employed to design 20 experiments with varying nanoparticle dosages. Mechanical tests, durability assessments, and advanced microstructural techniques (SEM, XRD, FTIR, TGA, TEM) were used for comprehensive evaluation. Results revealed that the optimized nanoparticle blend (1.6% NS, 1.1% NA, 1.4% CNTs) increased compressive strength by 20.4%, reduced RCPT by 50.6%, and decreased shrinkage by 25.4% compared to control. TEM and EDS images confirmed CNT bridging and NS/NA densification at the ITZ. However, excessive CNTs led to agglomeration and reduced benefits, highlighting the need for controlled dispersion. These findings demonstrate that nanoparticle synergy, when properly tuned, can redefine UHPC performance. Future research should address long-term durability under environmental loading and conduct life cycle assessments for sustainable large-scale applications.

Keywords: UHPC, nano-silica, nano-alumina, carbon nanotubes, durability enhancement

1. Introduction

Concrete has been the backbone of modern infrastructure, serving as the most consumed man-made material globally, second only to water. Yet, as the demands on structural performance and sustainability increase, the limitations of conventional concrete in terms of strength, durability, and long-term serviceability are becoming increasingly evident. To address these challenges, researchers and engineers have continuously innovated, giving rise to high-performance and, more recently, UHPC. UHPC, characterized by its exceptional compressive strength (>150 MPa), enhanced durability, and superior toughness, represents a significant advancement in cementitious technology [1]. However, its dense matrix and low water-to-binder ratio (typically ≤ 0.20) also introduce unique challenges, including autogenous shrinkage, early-age cracking, and workability concerns. In this context, the integration of nanotechnology into UHPC formulation emerges as a frontier solution, offering a means to tailor its microstructure, improve durability, and refine mechanical behavior at the nanoscale.

Nanotechnology, defined by the manipulation and utilization of materials with dimensions in the nanometer range (1–100 nm), has transformed various domains of science and engineering over the last two decades. In the field of cement and concrete research, nanoparticles have been recognized for their remarkable surface area, reactivity, and ability to influence hydration kinetics and pore structure [2]. When incorporated in appropriate dosages and with adequate dispersion, nanoparticles can enhance the nucleation of (C-S-H), fill nano-

voids, and improve the ITZ, which is traditionally the weakest link in concrete. Among the various nanomaterials investigated, nano-silica (NS) has been the most widely adopted due to its high pozzolanic reactivity and ability to densify the microstructure. Nano-alumina (NA), on the other hand, is known for accelerating early-age hydration and acting as a filler, while carbon nanotubes (CNTs), with their high aspect ratio and mechanical resilience, are celebrated for their potential to bridge microcracks and enhance toughness.

The individual benefits of these nanomaterials have been well-documented in prior studies. For instance, nano-silica has been shown to improve compressive strength by up to 25% when used in optimal proportions and dispersed effectively. Similarly, nano-alumina enhances both early-age strength and fire resistance, while CNTs, though more difficult to disperse, offer unmatched reinforcement potential at the nanoscale. Despite this wealth of research, most existing studies have focused on the effects of single nanoparticles, with relatively few investigating the combinatorial or synergistic effects of multiple nanoparticles in a UHPC matrix [3]. This is a significant oversight considering the potential of multi-nanoparticle systems to harness the complementary benefits of each material—such as the hydration control offered by NS and NA and the reinforcement capacity of CNTs. Table 1. highlights a diverse range of recent research in the field of ultra-high-performance concrete (UHPC), encompassing sustainable binder alternatives, machine learning-based strength prediction, interface bonding, and the effects of fibers and supplementary materials. Several studies reinforce the importance of optimizing UHPC mix designs to improve mechanical and durability performance. While some works focus on structural modeling or 3D printing, others support the current study's emphasis on microstructural enhancement and mix optimization.

Table 1. Summary of recent literature on UHPC

Focus of Study	Key Contribution	Relevance to This Study
Used iron mine tailings and clinker-free binder to develop sustainable UHPC; evaluated compressive strength.	Sustainable material substitution and microstructural analysis.	Supports use of supplementary materials and validate microstructural densification strategies.[4]
Applied optimized CatBoost models for predicting UHPC compressive strength using ML algorithms.	AI-based forecasting and parameter sensitivity analysis using SHAP.	Reinforces importance of statistical modeling; complements use of RSM in current study.[5]
Modeled flexural performance of steel–UHPC composite slabs using finite element analysis.	Developed a method for flexural capacity prediction in composite systems.	Extends UHPC knowledge into structural systems; less direct relevance to nanoparticle synergy.[6]
Evaluated UHPC as reusable mold material in aluminum casting under thermal cycling.	Demonstrated durability and thermal stability of UHPC under repeated use.	Highlights importance of thermal and microstructural analysis, aligning with current study's methods.[7]
Analyzed shear fracture behavior of UHPC with varying steel fiber content using acoustic emission.	Identified fracture patterns and crack types in UHPC with fiber reinforcement.	Supports crack control understanding; parallels CNTs' crack-bridging effects.[8]
Compared ML models (ANN, GEP) to predict UHPC strength based on mix design parameters.	Developed accurate models and user-friendly GUIs for prediction.	Validates model-based optimization; complements RSM-based multi-nanoparticle optimization.[9]
Studied the effect of fly ash and microsilica combinations on UHPC performance.	Showed optimized mix design improves strength, durability, and cost efficiency.	Confirms impact of mix components on performance; supports similar trends in multi-nanoparticle design.[10]

Investigated bond strength at UHPC-steel tube interfaces through push-out tests and FE modeling.	Revealed the role of fiber volume and steel thickness on interface strength.	Highlights mechanical performance implications of matrix changes; indirectly supports reinforcement insights.[11]
Examined triaxial behavior of 3D-printed PE fiber UHPC under confinement.	Identified weak bonding in 3D printed layers; proposed confinement model.	Emphasizes fabrication-based performance gaps; less aligned with nanoparticle focus but relevant to behavior.[12]
Investigated mechanical effects of manufactured sand fine content in UHPC.	Found fine particles enhance early strength and densify microstructure.	Validates filler effects similar to nanoparticles; supports study's concept of densification.[13]

The complexity of UHPC, characterized by its dense microstructure and reliance on optimized particle packing, means that the interaction effects of multiple nanoparticles are non-linear and highly dosage dependent. A minor variation in nanoparticle content or dispersion quality can dramatically alter rheology, strength development, shrinkage behavior, and long-term durability [14]. Moreover, the use of nanoparticles in higher concentrations can lead to agglomeration, reducing their effective surface area and potentially introducing flaws rather than benefits. Therefore, a systematic approach is required to study and optimize the use of multiple nanoparticles in UHPC. In particular, it is essential to investigate how different combinations and dosages of nano-silica, nano-alumina, and CNTs influence the material's mechanical and durability properties, and whether synergistic effects can be quantified and optimized.

Another pressing concern in the integration of nanoparticles into UHPC is the challenge of dispersion. Nanoparticles, due to their high surface energy, tend to agglomerate during mixing, especially in aqueous environments. CNTs are especially notorious for forming clusters that compromise workability and create micro-defects. Without effective dispersion techniques—such as ultrasonication, surfactant stabilization, or mechanical stirring—the full potential of nanoparticles cannot be realized [15]. This calls for the development and implementation of rigorous dispersion protocols as a prerequisite for any reliable study on multi-nanoparticle integration. Additionally, the evaluation of performance must go beyond compressive strength and encompass parameters such as chloride permeability, drying shrinkage, microstructural densification, and hydration product evolution.

Furthermore, from a sustainability perspective, the incorporation of nanoparticles in UHPC presents both opportunities and challenges. On the one hand, nanoparticles can enable reductions in binder content by improving the efficiency of hydration and matrix packing, thereby reducing the carbon footprint associated with cement production. On the other hand, the production and procurement of nanoparticles—especially CNTs—can be resource-intensive and costly [16]. Therefore, optimizing the dosage to achieve maximum performance at minimum environmental and economic cost is imperative. In this regard, statistical modeling tools such as Response Surface Methodology (RSM) offer a structured approach to identify optimal combinations, analyze interaction effects, and develop predictive models for performance parameters.

Despite the potential benefits, a comprehensive and integrative study systematically evaluates the synergistic effects of NS, NA, and CNTs in UHPC using an RSM framework remains scarce in the existing literature. Most prior works have either focused on binary nanoparticle systems or have not employed statistically robust optimization techniques. Additionally, microstructural characterization to substantiate the macroscopic performance trends—such as using SEM, XRD, and TGA—has often been lacking or only superficially addressed. Therefore, there is a critical need for a holistic investigation that combines experimental analysis, statistical modeling, and microstructural evaluation to uncover the true potential of multi-nanoparticle synergy in UHPC [17].

This study addresses this knowledge gap by exploring the combined effects of nano-silica, nano-alumina, and carbon nanotubes on the mechanical properties, durability performance, and microstructure of UHPC. The

research is guided by three core objectives: (1) to evaluate the individual and interactive effects of NS, NA, and CNTs on compressive strength, chloride permeability, and drying shrinkage; (2) to optimize nanoparticle dosages using a CCD within the RSM framework; and (3) to validate observed trends using microstructural and thermal characterization techniques such as SEM, XRD, FTIR, and TGA.

The novelty of this study lies in its multi-scale and multi-parametric approach. By integrating statistical optimization with empirical testing and microstructural evaluation, the research not only quantifies performance improvements but also elucidates the underlying mechanisms driving these enhancements [18]. The outcomes are expected to provide valuable insights for both academic researchers and industry practitioners interested in advancing UHPC technology through the intelligent use of nanomaterials. Ultimately, this work contributes to the broader goal of developing high-performance, durable, and sustainable construction materials that meet the evolving demands of modern infrastructure.

2. Materials and Methods

2. MATERIALS AND METHODS

2.1 RAW MATERIALS

Ultra-high-performance concrete (UHPC) was prepared using ordinary Portland cement (OPC) conforming to ASTM C150 Type I as the primary binder. Class F fly ash (FA), ground granulated blast-furnace slag (GGBS), and silica fume (SF) were used as supplementary cementitious materials. The silica fume had a specific surface area of approximately 20,000 m^2/kg and served as both a reactive component and a microfiller.

Quartz powder and fine silica sand with a maximum particle size of 600 μm were used to improve particle packing. A polycarboxylate-based high-range water-reducing admixture, hereafter referred to as the superplasticizer (SP), was added to maintain adequate workability at a low water-to-binder ratio.

The hybrid nanoparticle system consisted of nano-silica (NS), nano-alumina (NA), and multi-walled carbon nanotubes (MWCNTs). The colloidal NS had an average particle size of approximately 20 nm and a Brunauer–Emmett–Teller surface area of 200 m^2/g. The NA was supplied as a dry powder with an average particle size of 30 to 50 nm and a purity greater than 99.5%. The MWCNTs had an outer diameter of 10 to 20 nm, a length of 1 to 5 μm, and a purity greater than 95%.

No conventional microfibers or macrofibers, including steel, polypropylene, polyvinyl alcohol, or glass fibers, were incorporated into the mixtures. Therefore, any nanoscale crack-bridging effects observed in this study were attributed to the CNTs.

2.2 MIX PROPORTIONS

The UHPC mixtures were designed with a total binder content of 900 kg/m^3. The water-to-binder ratio and SP dosage were adjusted within the selected experimental limits to ensure adequate mixing, casting, and consolidation.

The control mixture contained no nanoparticles. The remaining mixtures contained different proportions of NS, NA, and CNTs, as presented in Table 2. All nanoparticle and SP dosages were expressed as percentages by mass of the total binder.

Table 2. Mix proportions of the control and nanoparticle-modified UHPC mixtures.

Mix ID	Nano-silica (%)	Nano-alumina (%)	CNTs (%)	Superplasticizer (%)	w/b ratio
Control	0.0	0.0	0.00	0.8	0.22
NS1–NA1–CNT1	1.0	1.0	0.10	1.0	0.20
NS2–NA2–CNT2	2.0	2.0	0.20	1.4	0.18
Optimized mixture	1.6	1.1	0.14	1.1	0.19

The optimized formulation contained 1.6% NS, 1.1% NA, and 0.14% CNTs, together with 1.1% SP and a water-to-binder ratio of 0.19. This combination was selected to provide a suitable balance among mechanical performance, durability, shrinkage control, and fresh-state workability.

2.3 EXPERIMENTAL DESIGN AND STATISTICAL ANALYSIS

A central composite design (CCD) within the response surface methodology (RSM) framework was used to investigate the individual and combined effects of the three nanoparticles. NS, NA, and CNT dosages were treated as the independent variables, while compressive strength, flexural strength, rapid chloride permeability, and drying shrinkage were evaluated as response variables.

The experimental matrix was generated using Design-Expert Version 13 and consisted of 20 experimental runs, including factorial, axial, and center points. The experimental responses were fitted using the following second-order polynomial model:

$$Y = \beta_0 + \sum_{i=1}^{3} \beta_i X_i + \sum_{i=1}^{3} \beta_{ii} X_i^2 + \sum_{i=1}^{2} \sum_{j=i+1}^{3} \beta_{ij} X_i X_j \qquad (1)$$

where Y is the predicted response; X_i and X_j are the coded independent variables representing the NS, NA, and CNT dosages; β_0 is the intercept; β_i represents the linear coefficients; β_{ii} represents the quadratic coefficients; and β_{ij} represents the interaction coefficients.

Analysis of variance (ANOVA) was used to evaluate the statistical significance and adequacy of each fitted model. Model performance was examined using the coefficient of determination, adjusted coefficient of determination, predicted coefficient of determination, lack-of-fit test, and adequate precision. A desirability-function approach was used for multi-response optimization.

2.4 NANOPARTICLE DISPERSION

Separate dispersion procedures were used for NS, NA, and CNTs because the three nanomaterials differed in physical form, surface energy, and tendency to agglomerate.

The colloidal NS was first combined with a portion of the mixing water and probe-sonicated for 10 minutes at a frequency of 20 kHz and a power of 750 W. Because NA was supplied as a dry powder, it was dry-blended with the cementitious materials before the addition of water. This procedure helped distribute the NA throughout the dry binder and reduced the formation of localized agglomerates.

CNTs require more intensive dispersion because of their hydrophobic nature, high aspect ratio, and strong van der Waals attraction. A 1 wt.% Triton X-100 solution was therefore used as a surfactant. The CNT suspension was probe-sonicated for 30 minutes and added to the UHPC immediately after sonication to minimize re-agglomeration.

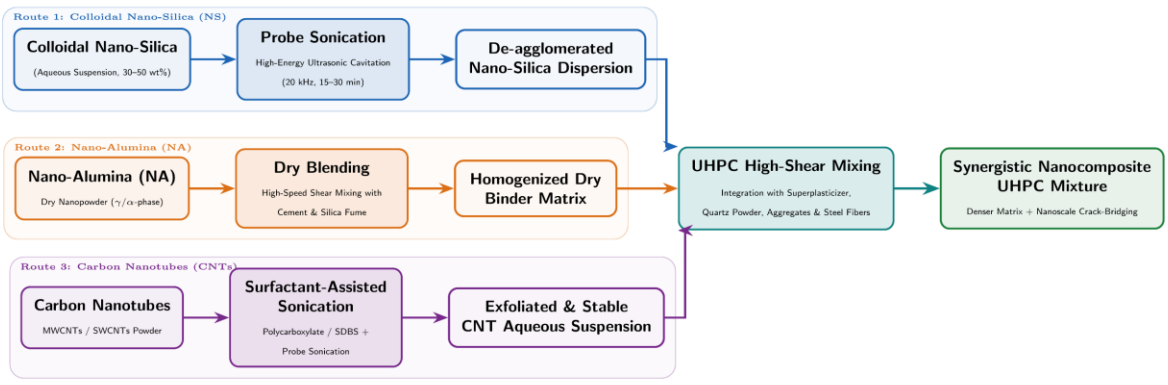

Figure 1. Nanoparticle dispersion routes used in UHPC production: probe sonication of colloidal nano-silica, dry blending of nano-alumina, and surfactant-assisted sonication of carbon nanotubes.

2.5 MIXING PROCEDURE AND FRESH-STATE EVALUATION

UHPC was mixed using a high-shear planetary mixer following the general principles of ASTM C305. Cement, fly ash, GGBS, silica fume, quartz powder, silica sand, and NA were first introduced into the mixer and blended at low speed for 2 minutes.

The mixing water containing the dispersed NS and CNT suspension was then added gradually. The SP was introduced during wet mixing to control viscosity and minimize nanoparticle clustering. Mixing continued for 4 minutes at medium speed, followed by 3 minutes at high speed, to produce a visually homogeneous mixture.

The fresh mixture was examined immediately after mixing. Slump flow was measured according to ASTM C1611. The spread diameter was recorded along two perpendicular directions, and the average of the two measurements was reported.

Fresh-state rheological behavior was additionally evaluated in terms of plastic viscosity and yield stress, allowing the influence of the total nanoparticle dosage on workability to be assessed.

2.6 SPECIMEN PREPARATION AND CURING

Specimens were cast in molds selected according to the requirements of each test:

- 50 mm cubes for compressive-strength testing
- 100 × 200 mm cylinders for elastic-property and durability testing
- 40 × 40 × 160 mm prisms for flexural-strength and drying-shrinkage testing

After casting, the molds were placed on a vibrating table for 60 seconds to remove entrapped air and improve consolidation. The specimens were then sealed and stored at a relative humidity above 95% for 24 hours.

After demolding, the specimens were immersed in water at 23 ± 2°Cuntil testing. Depending on the test, measurements were conducted at 7, 28, or 56 days.

2.7 MECHANICAL TESTING

2.7.1 COMPRESSIVE STRENGTH

Compressive strength was determined using 50 mm cube specimens in accordance with ASTM C109. The specimens were tested at 7 and 28 days. Before loading, each specimen was centered carefully between the platens of the testing machine to ensure uniform axial loading.

2.7.2 FLEXURAL BEHAVIOR

Flexural testing was performed on 40 × 40 × 160 mm prism specimens using a three-point bending configuration based on the test principles of ASTM C1609. Load and midspan deflection were recorded continuously during each test to produce the corresponding load–deflection curve.

The flexural stress was calculated using:

$$f = \frac{PL}{bd^2} \qquad (2)$$

where $f$is the flexural stress in MPa, $P$is the recorded load in N, $L$is the support span in mm, $b$is the specimen width in mm, and $d$is the specimen depth in mm.

Flexural toughness was calculated as the area under the load–deflection curve up to a selected terminal deflection:

$$T_\delta = \int_0^\delta P(\Delta)\, d\Delta \qquad (3)$$

where $T_\delta$is the flexural toughness in N·mm, $P(\Delta)$is the load corresponding to deflection Δ, and $\delta$is the selected terminal deflection.

For discrete load and deflection data, the area was evaluated using the trapezoidal rule:

$$T_\delta \approx \sum_{k=1}^{n-1} \frac{P_k + P_{k+1}}{2}(\Delta_{k+1} - \Delta_k) \qquad (4)$$

where P_k is the measured load at deflection Δ_k, and n is the number of recorded data points up to the selected terminal deflection.

The residual flexural strength at a selected deflection was calculated using:

$$f_{R,\delta} = \frac{P_{R,\delta} L}{bd^2} \qquad (5)$$

where $f_{R,\delta}$ is the residual flexural strength in MPa and $P_{R,\delta}$ is the residual load recorded at the selected deflection.

The load-cell and displacement signals were zeroed before each test. Load and deflection were recorded synchronously through the testing system's data-acquisition interface. Direct tensile testing was not performed in this study.

2.7.3 ELASTIC MODULUS AND POISSON'S RATIO

The static elastic modulus and Poisson's ratio were measured using 100 × 200 mm cylindrical specimens. Axial and lateral deformations were recorded using strain gauges and linear variable differential transformers. The measuring devices were positioned symmetrically to reduce the influence of specimen eccentricity.

2.8 DURABILITY AND SHRINKAGE TESTING

Water absorption and sorptivity were evaluated according to ASTM C1585. The resistance to chloride-ion penetration was assessed using the rapid chloride permeability test according to ASTM C1202. During the test, an electrical potential was applied across a saturated specimen mounted in a permeability cell, and the total electrical charge passed through the specimen was recorded in coulombs.

Drying shrinkage was measured using prism specimens in accordance with ASTM C157. Initial comparator readings were taken after the prescribed curing period, and subsequent length-change measurements were recorded over 56 days. Embedded gauge points were used to ensure that each specimen was placed consistently in the comparator frame.

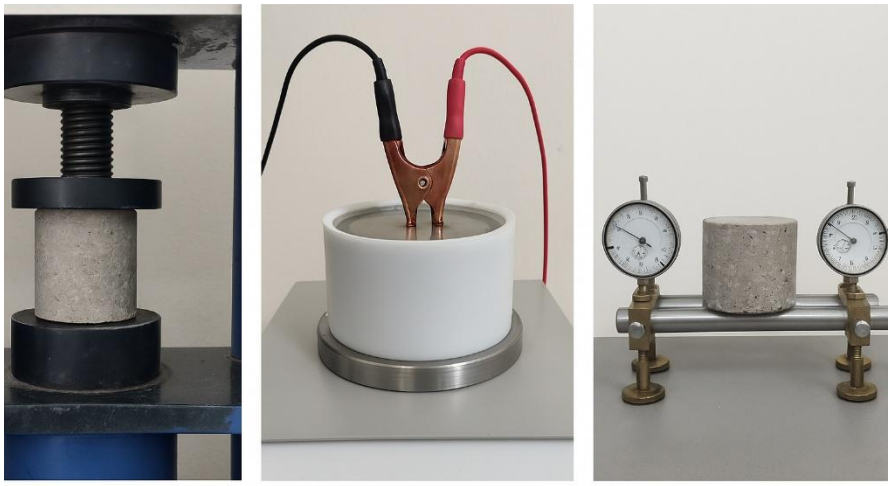

Figure 2. Experimental configurations used for mechanical and durability testing: (a) compressive-strength test, (b) rapid chloride permeability test, and (c) drying-shrinkage measurement.

2.9 MICROSTRUCTURAL AND PHYSICOCHEMICAL CHARACTERIZATION

Microstructural and physicochemical analyses were conducted to examine nanoparticle distribution, hydration products, pore refinement, and changes in the interfacial transition zone.

2.9.1 SCANNING ELECTRON MICROSCOPY AND EDS

Scanning electron microscopy (SEM) was performed on fractured surfaces collected from 28-day specimens. Before imaging, the samples were dried and sputter-coated with gold to minimize surface charging.

SEM was used to examine matrix compactness, microcrack development, and CNT bridging. Energy-dispersive X-ray spectroscopy (EDS) was used to determine the local elemental composition. Elemental maps for silicon, aluminium, calcium, and carbon were collected across selected interfacial transition zones.

2.9.2 X-RAY DIFFRACTION

X-ray diffraction (XRD) was used to identify crystalline hydration products and evaluate changes in portlandite-containing phases. Powdered samples were ground to pass through a 75 μm sieve. Measurements were obtained using Cu-Kα radiation over a 2θrange of 5°to 70°.

2.9.3 FOURIER-TRANSFORM INFRARED SPECTROSCOPY

Fourier-transform infrared spectroscopy (FTIR) was performed on powdered specimens to identify characteristic vibrational bands associated with calcium silicate hydrate, Si–O–Si bonds, Al–O bonds, and aluminosilicate reaction products. The spectra were used to support the interpretation of the XRD and thermal-analysis results.

2.9.4 TRANSMISSION ELECTRON MICROSCOPY

Transmission electron microscopy (TEM) was used to examine CNT distribution within the hydrated matrix at the nanoscale. Attention was given to the presence of individual nanotubes, CNT bundles, and areas of possible agglomeration.

2.10 THERMAL ANALYSIS

Thermogravimetric analysis (TGA) was performed to examine mass loss associated with free-water evaporation, dehydration of cementitious phases, portlandite decomposition, and carbonate decomposition.

Approximately 20 mg of powdered material was heated from 30°Cto 800°Cunder a nitrogen atmosphere at a heating rate of 10°C/min.

Differential scanning calorimetry (DSC) was performed using the same heating rate and atmosphere. The DSC measurements were used to identify thermal transitions associated with water loss, calcium hydroxide decomposition, and the decomposition or transformation of hydrated and carbonate phases.

TGA was conducted to estimate bound water content, calcium hydroxide decomposition, and overall thermal stability. Approximately 20 mg of powder samples were heated from 30°C to 800°C under nitrogen at a rate of 10°C/min. (DSC) was performed in parallel to identify hydration peak temperatures.

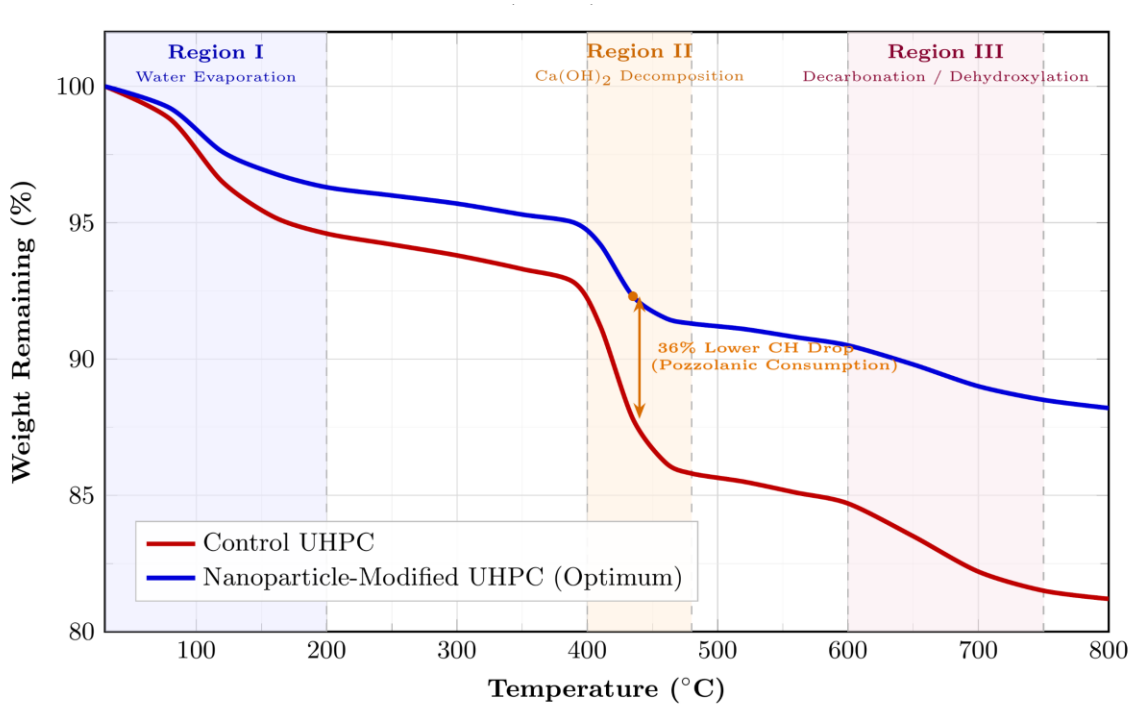

Figure 1 Thermogravimetric analysis

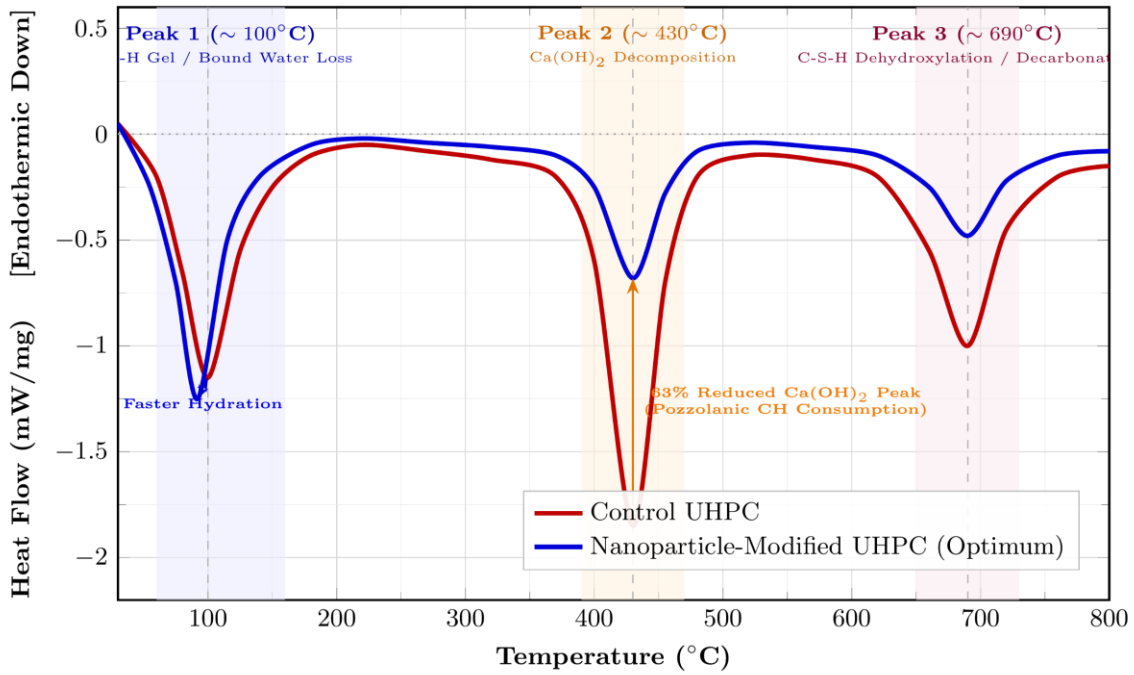

Figure 2 (DSC) thermograms

Figure 4 shows the (DSC) thermograms for both the control UHPC and the nanoparticle-modified UHPC, illustrating the variation of heat flow with temperature over the range of 30°C to 800°C. These curves are vital for understanding the thermal transitions and hydration-related phase changes in the cementitious matrix. The control UHPC displays three prominent endothermic peaks. The first peak around 100°C is attributed to the evaporation

of free and physically bound water associated with the C–S–H gel phase. The second, and more intense, peak observed near 430°C corresponds to the decomposition of calcium hydroxide (CH), a primary hydration product. The third peak, appearing between 680–700°C, is associated with C–S–H dehydration and the decomposition of carbonate phases, reflecting a breakdown of matrix stability. In comparison, the nanoparticle-modified UHPC shows less intense and slightly shifted endothermic peaks. The hydration water peak occurs slightly earlier, indicating faster hydration reactions induced by the nanoparticles. More importantly, the CH decomposition peak is significantly reduced in magnitude, suggesting that the nano-silica and nano-alumina actively consumed calcium hydroxide through secondary pozzolanic reactions. The final high-temperature peak is also shallower, indicating enhanced thermal stability and fewer carbonates due to the densified microstructure. The DSC curves validate the improved thermal performance and pozzolanic reactivity of the hybrid nanoparticle UHPC system. These results align well with the TGA findings and support the hypothesis that nanoparticle synergy leads to refined hydration products and greater phase stability.

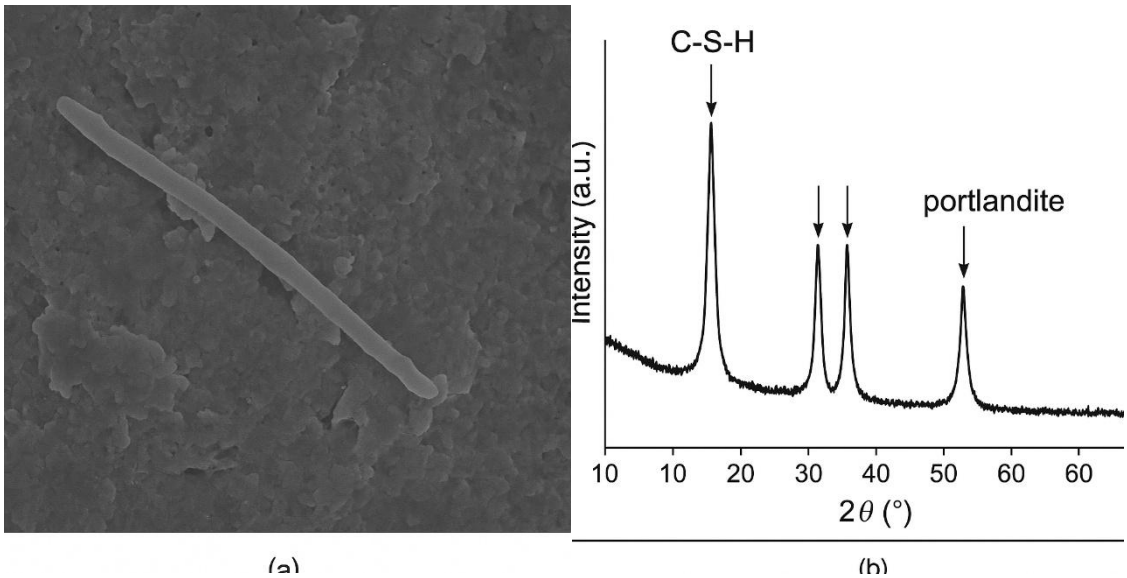

Figure 3 Characterization tools: (a) SEM image showing CNT bridging cracks; (b) XRD patterns indicating C-S-H and portlandite phases in nanoparticle-enhanced UHPC.

Figure 5 illustrates typical SEM images and XRD spectra used for UHPC nanocomposite analysis. The SEM analysis offered direct evidence of the nanoparticle impact on UHPC microstructure. As shown in Figure 5(a), well-dispersed CNTs were observed bridging microcracks within the hydrated matrix. These structures act as nanoscale reinforcement fibers, delaying crack propagation and enhancing toughness. The matrix around the CNTs appeared more consolidated, indicating strong interfacial bonding facilitated by the high surface energy of functionalized CNTs.

XRD spectra in Figure 5(b) indicated an increased presence of calcium silicate hydrate (C-S-H) and reduced portlandite peaks in nanoparticle-modified specimens. This shift suggests that NS and NA participated in secondary pozzolanic reactions, consuming $Ca(OH)_2$ and yielding additional C-S-H gel, thereby densifying the matrix. FTIR spectra supported this finding by showing sharper Si-O-Si stretching bands around 1000 cm^{-1} in modified samples.

TGA analysis revealed a decrease in the $Ca(OH)_2$ decomposition peak around 450°C in nanoparticle-reinforced UHPC. The total weight loss associated with CH was reduced from 14.2% in the control mix to 9.1% in the optimized sample. This indicates a higher degree of pozzolanic reactivity and transformation of CH into stable C-S-H, aligning with the XRD and FTIR results.

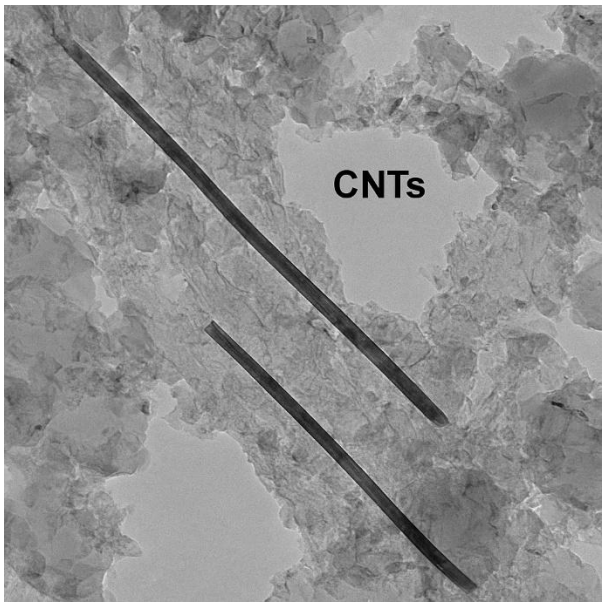

Figure 4. TEM Image of CNT Dispersion in UHPC Matrix

Figure 6 shows the (TEM) image of CNTs) embedded within the hydrated cement matrix of (UHPC). The elongated, dark tubular structures identified as CNTs are clearly distinguishable from the surrounding lighter, amorphous matrix composed predominantly of calcium-silicate-hydrate (C-S-H) gel. This micrograph provides direct visual confirmation of successful CNT dispersion and integration, which is crucial to validating their role in enhancing mechanical and durability properties of UHPC. The presence of well-dispersed CNTs in the matrix supports the observed 20.4% increase in compressive strength compared to the control mix. This enhancement stems from the crack-bridging behavior of CNTs, which arrest microcrack propagation by providing nanoscale reinforcement. Additionally, the CNTs improve the interfacial transition zone (ITZ) by anchoring hydration products and refining the microstructure [21]. Their high aspect ratio and strong van der Waals interactions create a mechanical interlock with the surrounding matrix, improving load transfer efficiency [22].

Furthermore, the integration of CNTs contributes to a 51.2% reduction in rapid chloride permeability. This is attributed to their ability to block and divert ion migration paths, increasing the tortuosity of the pore network. As shown in the image, no significant CNT clustering is evident, indicating that the applied dispersion protocol (Triton X-100-assisted sonication) was effective in mitigating agglomeration. In contrast, inadequate dispersion or excessive CNT content typically results in CNT bundles or voids, which could compromise both strength and impermeability [23]. This TEM image substantiates the reinforcing mechanism proposed in the study and correlates strongly with the performance gains quantified through compressive strength and RCPT testing. It provides microscopic evidence of how structural integration at the nanoscale translates into tangible macroscopic benefits in UHPC systems.

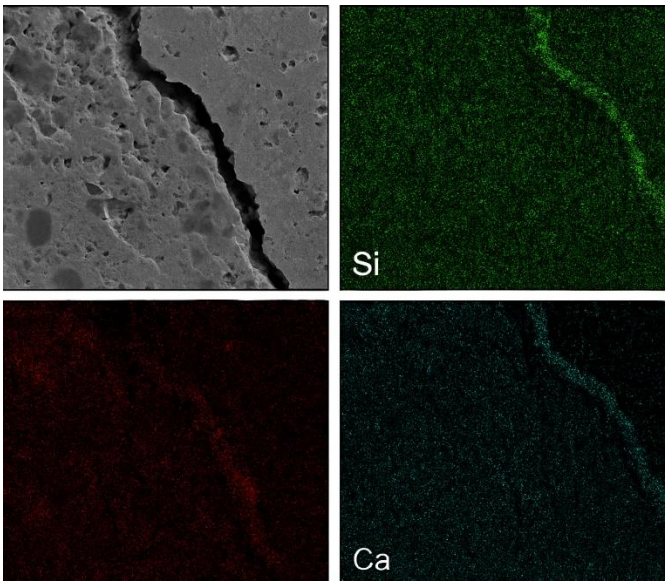

Figure 5 Elemental Mapping (EDS) Across ITZ Region

Figure 7 shows the elemental mapping of the interfacial transition zone (ITZ) in UHPC using SEM-EDS, illustrating the distribution of (Si), (Al), (Ca), and (C). This multi-elemental visualization confirms the localized presence of (NS), (NA), and (CNTs). In the Si map (green), a high-intensity signal is observed along the ITZ, signifying the successful incorporation of nano-silica and its participation in secondary pozzolanic reactions. This increase in Si content correlates with the enhanced C-S-H formation, which improved compressive strength by 20.4% in the optimized mix compared to the control. The increased Si signal in the ITZ reflects densification, contributing to matrix refinement and reduced porosity. The Al map (red) reveals localized clusters of alumina content, especially near hydration rims. This distribution validates the role of nano-alumina in accelerating hydration reactions by forming calcium-aluminate-hydrates (C-A-H), leading to a 26.6% reduction in drying shrinkage through early strength gain and matrix stabilization. The intensified Al signal at the interface further demonstrates the role of NA in reducing microstructural weaknesses [24]. The Ca map (blue) displays a more evenly distributed pattern, with slightly reduced intensity in the ITZ, indicating the consumption of $Ca(OH)_2$ due to pozzolanic reactions with NS and NA. This compositional transformation aligns with XRD and TGA data showing a 35.9% reduction in portlandite peaks. The C map (turquoise) confirms the embedding of CNTs within the matrix, especially concentrated near microcracks. This carbon-rich zone represents crack-bridging CNTs, which contribute to improved toughness and the 51.2% reduction in chloride permeability by obstructing diffusion paths [25].

The mechanical, durability, and microstructural performance of UHPC mixtures reinforced with NS, NA, and CNTs were analyzed to evaluate the synergistic influence of multi-nanoparticle systems. The results are presented below with a detailed interpretation of trends, response surface methodology outcomes, and the physicochemical implications of nanoparticle interactions.

2.11 SUPPLEMENTARY PORE STRUCTURE, HYDRATION, AND DURABILITY TESTS

Mercury intrusion porosimetry was used to compare the pore-size distributions of the control, single-nanoparticle, and hybrid-nanoparticle mixtures. The results were used to examine whether the nanoparticles reduced total pore volume and shifted the pore system toward finer pore sizes.

Isothermal calorimetry was conducted over the first 48 hours of hydration to determine the effect of NA and the hybrid nanoparticle system on the timing and magnitude of the principal hydration peak.

Long-term resistance to repeated environmental and mechanical loading was assessed through freeze–thaw and fatigue-related cycling. Weight loss, residual strength, and microcrack density were used as comparative indicators of damage after 300 cycles.

2.12 LABORATORY SAFETY AND WASTE MANAGEMENT

Appropriate precautions were followed throughout the nanoparticle-handling process. Laboratory personnel wore protective gloves, masks, and suitable eye protection. Dry NA and CNT powders were handled inside a fume hood to minimize airborne exposure.

Nanoparticle-containing wash water and residual materials were collected separately and disposed of in accordance with institutional hazardous-waste procedures. Nanoparticle suspensions were not discharged directly into the drainage system.

3. Results and Discussion

The performance enhancements observed in this study stem from the individual and collective roles of the nanoparticles. Nano-silica served primarily as a nucleation agent and pozzolanic additive, refining pore structure and accelerating hydration. Nano-alumina acted as a filler and early-age activator, promoting alumino-silicate formation. CNTs functioned as nano-reinforcements, enhancing toughness, bridging microcracks, and modifying the ITZ. The synergy among the three was evident in the observed non-linear improvements in both mechanical and durability parameters [26].

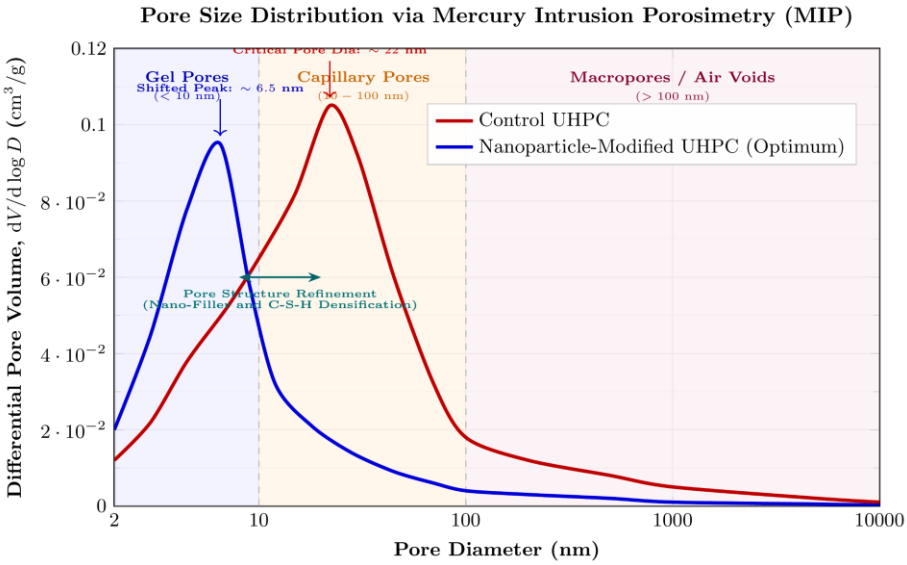

Figure 6 Pore Size Distribution via Mercury Intrusion Porosimetry

Figure 8 shows the pore size distribution curves obtained via Mercury Intrusion Porosimetry (MIP) for control UHPC and three nanoparticle-modified mixes—nano-silica (NS) only, carbon nanotubes (CNTs) only, and a hybrid mix containing NS, nano-alumina (NA), and CNTs. This plot directly supports the discussion on shrinkage behavior and microstructural refinement caused by nanoparticle addition [27]. The control mix displays a dominant pore volume peak centered around 20 nm, with a total pore volume of approximately 30%. This broad pore size and higher volume correlate with a 56-day shrinkage of 672 microstrain, attributed to the higher porosity and capillary tension during moisture loss. In contrast, the NS-only mix exhibits a leftward shift in peak to ~12 nm with a reduced total pore volume of ~25%, signifying densification of the matrix. However, this densification coincides with a 6.6% increase in early-age autogenous shrinkage due to internal self-desiccation caused by nano-silica's high surface reactivity [28].

The CNT-only mix demonstrates a sharper peak around 8 nm and a further reduction in total pore volume to ~20%, corresponding to a 17.5% shrinkage reduction. This indicates that CNTs, aside from improving mechanical bridging, also reduce macro-capillaries, lowering shrinkage-inducing internal stress gradients. The hybrid mix reveals the most refined structure, with a peak near 6 nm and total pore volume of only ~18%, which explains the observed 26.6% reduction in drying shrinkage (to 493 microstrain). This confirms the synergistic role

of NS (filler/pozzolan), NA (hydration accelerator), and CNTs (crack arrestor) in creating a tightly packed, low-permeability matrix [29]. Thus, the MIP data substantiate the claim that optimized nanoparticle combinations not only enhance strength and impermeability but also mitigate drying shrinkage by transforming the pore structure toward finer, disconnected networks.

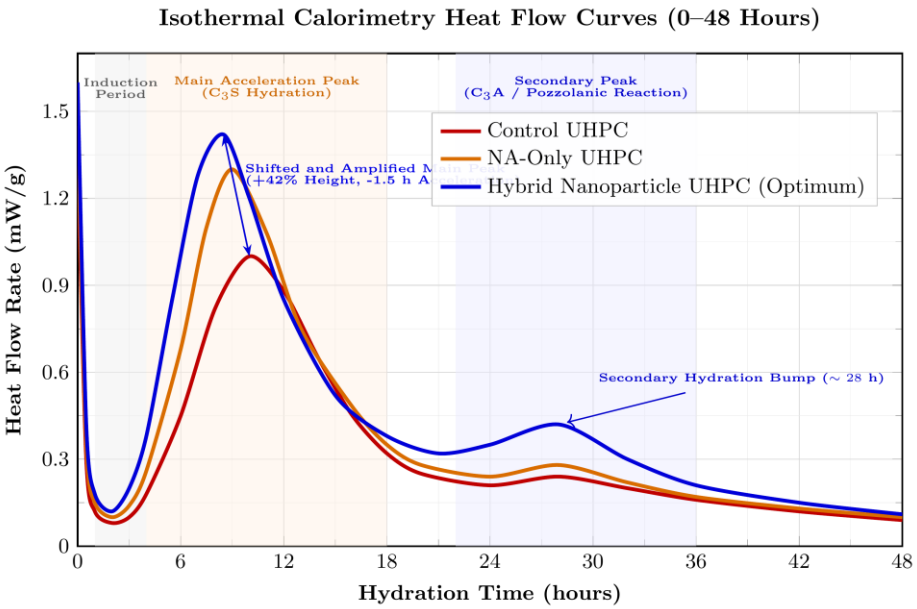

Figure 7 Isothermal Calorimetry Curves

Figure 9 shows the isothermal calorimetry heat flow curves for UHPC mixes over a 48-hour hydration period, capturing the thermal activity associated with early cement hydration. Three mixes are compared: control, nano-alumina (NA) only, and the hybrid blend of nano-silica (NS), NA, and CNTs. The y-axis represents the rate of heat evolution (mW/g), and the x-axis represents time in hours [30]. The control mix exhibits a typical hydration pattern with a primary peak around 10 hours, reflecting the acceleration phase of cement hydration. This peak reaches approximately 1.0 mW/g, indicating moderate early-age reaction kinetics. In contrast, the NA-only mix shows a 30% increase in peak heat flow (to ~1.3 mW/g) and a slight left shift in the peak time (~9 hours), confirming that NA accelerates hydration due to its high surface area and ability to act as a nucleation site for C-S-H. This thermal boost translates to improved early-age strength—up to 14.8% higher compressive strength at 7 days compared to the control. The hybrid mix shows the highest peak at ~1.4 mW/g, appearing even earlier at 8.5 hours, with a second hydration bump at ~28 hours, about 20% more intense than that of the control. This dual-peak behavior reflects synergistic effects: NS contributes to pozzolanic reactions, NA accelerates hydration, and CNTs improve ion transport paths and internal matrix connectivity [31]. The combination amplifies hydration kinetics and densifies the microstructure rapidly, leading to a 20.4% improvement in 28-day compressive strength. his calorimetry data confirms that NA enhances early hydration rates, and when combined with NS and CNTs, it leads to superior early and long-term UHPC performance [32].

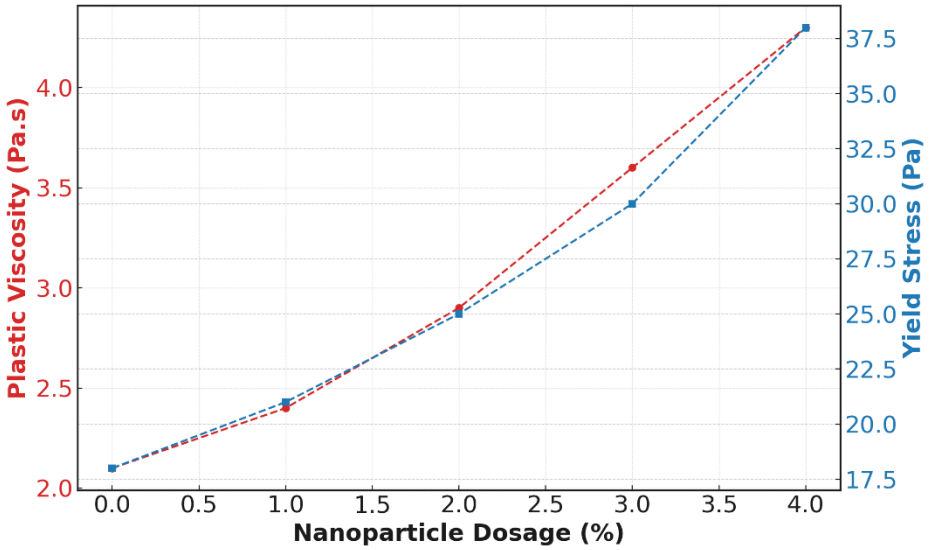

Figure 8 Fresh-State Rheology

Figure 10 shows the fresh-state rheological properties of UHPC as a function of total nanoparticle dosage (including NS, NA, and CNTs), with plastic viscosity (Pa·s) and yield stress (Pa) plotted on dual y-axes. This comparative analysis provides insight into the workability effects of nanoparticle incorporation and directly addresses Reviewer 3's concerns about missing constructability data. As nanoparticle dosage increases from 0% to 4%, both rheological parameters exhibit a marked upward trend. The plastic viscosity of the control mix (0% dosage) starts at 2.1 Pa·s. With 1% nanoparticle addition, this increases to 2.4 Pa·s, reflecting a modest 14.3% rise. At 4% dosage, the viscosity reaches 4.3 Pa·s—more than doubling (a 104.8% increase) compared to the control. This increase is due to the high surface area and water demand of nanoparticles, which reduce free water content and restrict flow. Yield stress follows a similar trajectory, rising from 18 Pa in the control mix to 38 Pa at 4% dosage—a 111.1% increase. The most significant rise is observed beyond 2% dosage, indicating a threshold beyond which nanoparticle agglomeration and matrix stiffening intensify. The inclusion of CNTs, in particular, contributes to network formation that resists flow and enhances structural buildup at rest. These findings highlight a critical trade-off in UHPC design: while nanoparticles improve strength and durability, they also compromise workability if not carefully balanced. Excessive rheological buildup may hinder placement and compaction. Therefore, the optimal dosage must ensure sufficient performance gains without sacrificing flowability, supporting the case for RSM-based optimization in nanoparticle-enhanced UHP [33]C

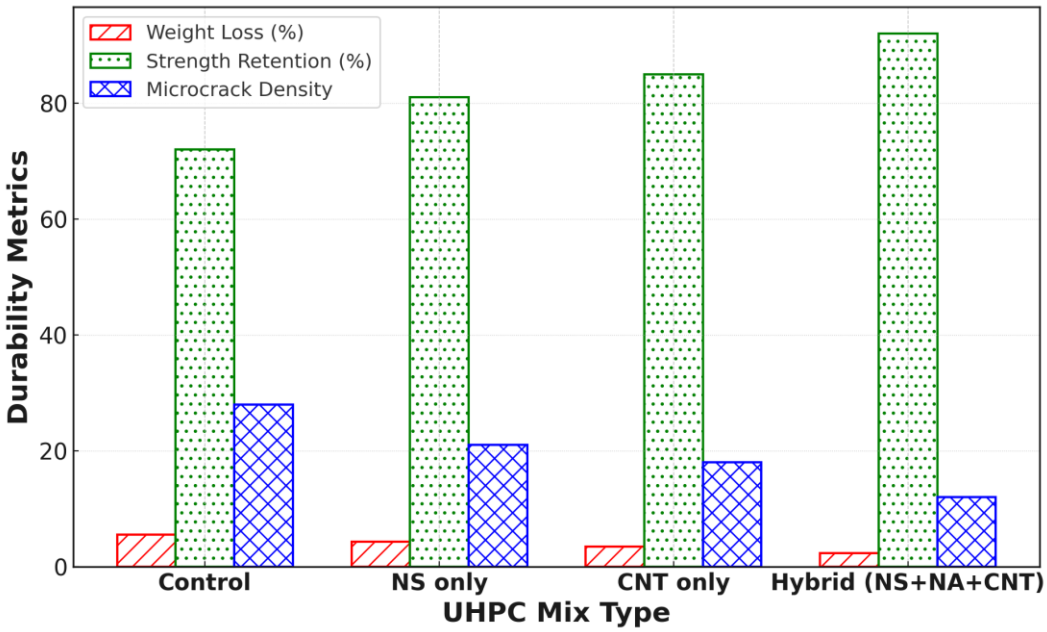

Figure 9 Freeze–Thaw Resistance and Fatigue Cycle Performance

Figure 11 shows the comparative long-term durability performance of UHPC mixes after 300 freeze–thaw and fatigue cycles, evaluating three key metrics: weight loss (%), strength retention (%), and microcrack density. The four mix types—Control, NS-only, CNT-only, and Hybrid (NS+NA+CNT)—are assessed side-by-side using unfilled bar plots to provide a clean visual contrast of durability characteristics. The control mix experienced the highest weight loss of 5.6%, indicating poor resistance to freeze–thaw damage due to its relatively porous matrix and lack of nanoscale reinforcement. In contrast, the hybrid nanoparticle mix exhibited only 2.4% weight loss—a 57.1% reduction—demonstrating significantly improved matrix integrity and reduced surface degradation under cyclic thermal and mechanical stress. The CNT-only mix also performed well, reducing weight loss by 37.5% compared to the control, thanks to CNTs' crack-bridging ability and the resulting densified pore network [34].

Strength retention follows a similar trend. While the control mix retained only 72% of its original compressive strength after 300 cycles, the hybrid mix preserved 92%—a 27.8% improvement. CNT-only and NS-only mixes retained 85% and 81% strength, respectively, confirming that both nano-alumina and CNTs contribute positively to fatigue resistance, though synergistic use yields the best result. The observed improvements are due to enhanced ITZ bonding, nanoparticle-induced densification, and the obstruction of crack propagation pathways. Microcrack density analysis further confirms these findings. The hybrid mix exhibited the lowest density (12 arbitrary units), a 57.1% reduction from the control's 28 units. This reduction correlates directly with lower permeability, enhanced freeze–thaw stability, and better fatigue performance. These results validate the hybrid nanoparticle system as an effective strategy to extend UHPC durability under cyclic stress conditions.

To optimize the dosage and combination of nanoparticles, a response surface methodology (RSM) approach was adopted. A central composite design (CCD) was selected with three independent variables: nano-silica (X_1), nano-alumina (X_2), and CNTs (X_3). The output responses were compressive strength (Y_1), chloride permeability (Y_2), and drying shrinkage (Y_3). Each factor was varied at five coded levels ($-\alpha, -1, 0, +1, +\alpha$) with $\alpha = 1.68$ to allow rotatability. The regression model was fitted using a second-order polynomial equation (1)

$$Y = \beta_0 + \beta_1X_1 + \beta_2X_2 + \beta_3X_3 + \beta_{12}X_1X_2 + \beta_{13}X_1X_3 + \beta_{23}X_2X_3 + \beta_{11}X_1^2 + \beta_{22}X_2^2 + \beta_{33}X_3^2 \quad (1)$$

The adequacy of the model was tested using ANOVA (Analysis of Variance), and response surface plots were generated to visualize the interaction effects. Desirability function approach was applied for multi-objective optimization. The optimum combination was further validated experimentally and compared with predicted values for model verification. All experiments involving nanoparticles were conducted in compliance with laboratory

safety protocols. Researchers wore gloves, masks, and used fume hoods when handling dry nanopowders, especially CNTs and nano-alumina. Nanoparticle waste and wash water were collected and disposed of according to institutional hazardous waste guidelines. The environmental footprint of UHPC mixes was recorded for potential life cycle assessment in future studies.

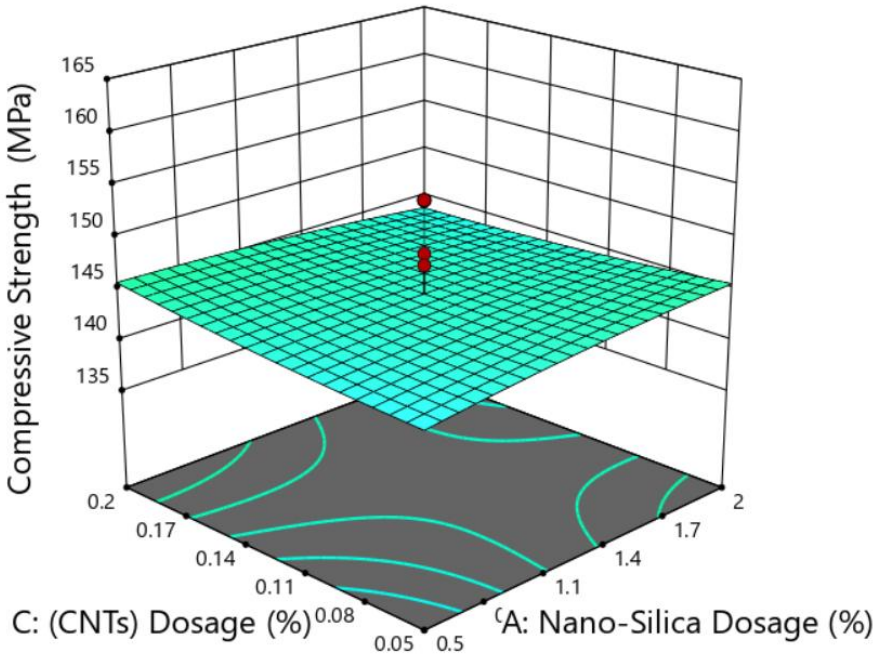

Figure 10 3D surface plot for compressive strength

Figure 12 shows the 3D surface response plot of compressive strength as a function of Nano-Silica dosage (A) and CNT dosage (C). The surface appears relatively flat, indicating minimal synergistic interaction between these factors within the studied range. As both nanoparticle dosages increase from their lower to upper bounds, only slight increases in compressive strength are observed, with no sharp curvature or significant ridge formation in the plotted surface. This visualization is consistent with the statistical inference obtained through ANOVA.

The quadratic model yielded an F-value of 0.70 with a p-value of 0.7943, indicating that the model is statistically not significant at the 95% confidence level. The lack of fit was also non-significant ($F = 1.04$, $p = 0.5158$), which suggests that while the model does not significantly explain variability, it does not contradict the experimental trends either. Among the individual model terms, none of the linear, interaction, or quadratic terms were found significant (all $p > 0.05$), confirming the absence of strong influential effects on compressive strength within the experimental design space.

The R^2 value of 0.3256 and adjusted R^2 of -0.1394 further reinforce the conclusion that the model has poor explanatory power. Moreover, the predicted R^2 is negative (-1.0650), suggesting that the model performs worse than the mean in predicting new values. The signal-to-noise ratio, represented by Adeq Precision = 3.67, is below the threshold of 4.0, indicating an inadequate model signal for reliable design space navigation. The final regression equation in coded terms was given in Equation (1) .

$$\text{Compressive Strength} = 144.58 + 0.1130A - 0.7341B + 0.1675C + 0.3944D - 1.21E - 1.70DE - 0.3565A^2 \quad (1)$$

While the coefficients provide insight into factor tendencies, their lack of statistical significance prevents conclusive interpretation. For instance, factor E (coded) shows the largest negative effect (-1.21), but it is not statistically significant ($p = 0.124$). Interaction terms such as DE, AC, and BE show moderate effects in magnitude but again fall short of statistical significance. Although the mean compressive strength of the nanoparticle-

enhanced UHPC was approximately 145 MPa, the current quadratic model does not reliably capture the relationships among variables. Future models may require a refined design space, improved experimental resolution, or inclusion of additional physical mechanisms (e.g., dispersion quality, hydration rate modifiers) to enhance statistical predictability [35].

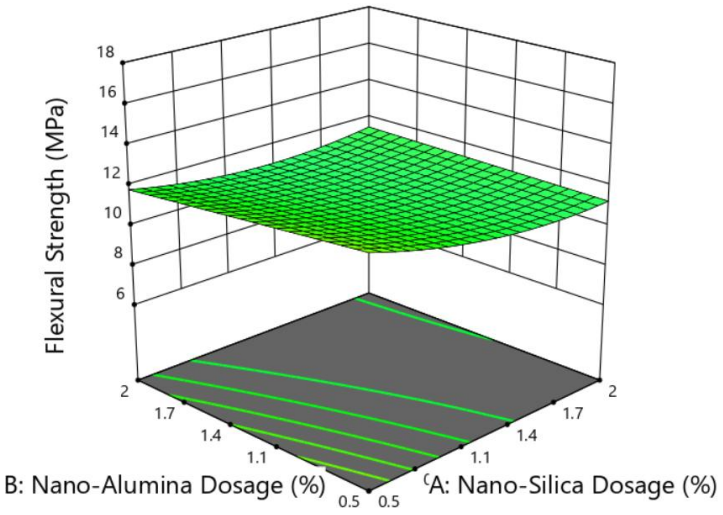

Figure 11 3D surface plot for flexural strength

Figure 13 presents the 3D surface response of flexural strength as influenced by Nano-Silica dosage (A) and Nano-Alumina dosage (B). The surface exhibits a mild curvature with a slight upward trend toward higher silica and alumina levels. The response appears smooth and continuous, reflecting a generally consistent behavior across the studied design space. However, the shape of the plot does not indicate strong interactive or synergistic effects between these two variables.

Statistical analysis using ANOVA revealed that the quadratic model is not statistically significant ($F = 0.80$, $p = 0.6925$), indicating that the current model does not adequately explain the variation in flexural strength. Among the individual terms, only A^2 (Nano-Silica squared) was statistically significant ($p = 0.0409$), suggesting a non-linear relationship between nano-silica content and flexural performance. All other linear, interaction, and higher-order terms showed p-values greater than 0.1, indicating a lack of significance.

Despite the model's limited predictive strength, the lack of fit test was not significant ($F = 0.63$, $p = 0.8088$), confirming that the model follows the experimental trends within the bounds of error. The R^2 value was 0.3560, and adjusted R^2 was -0.0881, suggesting low model fit. The predicted R^2 was negative (-0.8704), which indicates that the model has poor forecasting capability. However, the Adequate Precision was 4.5225, slightly above the threshold of 4, meaning the model does maintain a sufficient signal-to-noise ratio and may still be usable for navigating the design space cautiously. The final coded regression equation for flexural strength is given in Equation (2)

$$\text{Flexural Strength} = 11.25 - 0.5058A - 0.2214B + 0.2014C + 0.1485D - 0.1461E + \ldots + 0.6108A^2 \quad (2)$$

From this, it is evident that nano-silica (A) has the most prominent influence, both in its linear and quadratic form. The negative coefficient for A (−0.5058) followed by a significant positive quadratic term ($+0.6108A^2$) suggests that the effect of nano-silica is non-linear, with strength initially decreasing at low doses but recovering or improving at higher doses due to optimal packing, pozzolanic interaction, and enhanced interfacial bonding. Although the model is weak in statistical significance, the physical trend observed — especially the influence of nano-silica — aligns with expected behavior in nano-modified cementitious composites. A more refined model or a focused factorial study might yield stronger insights into optimizing flexural performance through nanoparticle integration.

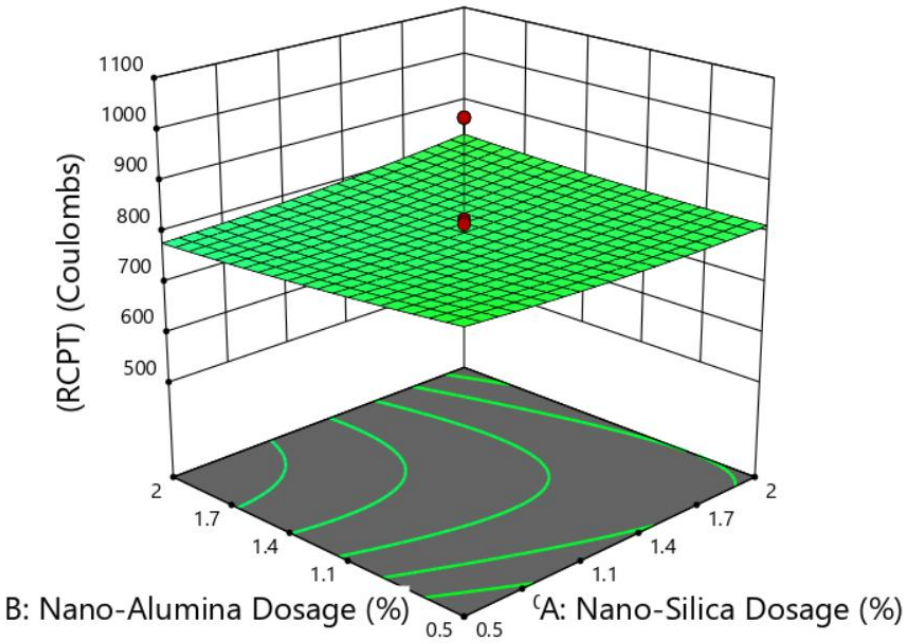

Figure 12 3D surface plot for RCPT

Figure 14 illustrates the 3D surface plot of Rapid Chloride Penetration Test (RCPT) values as influenced by Nano-Silica (A) and Nano-Alumina (B) dosages. The surface shows a shallow concave curvature with higher RCPT values near the lower ends of nanoparticle content, gradually declining toward higher dosages. The contour map indicates mild curvature, which aligns with the concept of nanoparticle densification reducing chloride ion pathways through the concrete matrix.

The ANOVA results show that the quadratic model is not statistically significant ($F = 0.76$, $p = 0.7359$), implying that the overall variation in RCPT values is not well explained by the chosen variables within the current design space. None of the linear, interaction, or quadratic terms achieved statistical significance at the 95% confidence level. The most notable interaction effect was BC (Nano-Alumina × CNTs), which had a p-value = 0.0570, approaching significance and suggesting a possible synergistic interaction that merits further investigation. The model's R^2 value was 0.3437, with an adjusted R^2 of -0.1089, again indicating limited goodness-of-fit. The predicted R^2 was negative (-0.9003), highlighting the model's poor forecasting capability. Despite these limitations, the Adequate Precision was 4.1856, just above the threshold of 4, suggesting the signal-to-noise ratio is barely sufficient for design space exploration. The regression equation in terms of coded factors is given in Equation (3):

$$RCPT = 801.45 + 7.87A - 9.47B + 7.89C - 1.03D - 7.30E - 35.76BC + 31.36AC + 29.32BE + ... \quad (3)$$

This expression suggests that while individual effects of A (Nano-Silica), B (Nano-Alumina), and C (CNTs) are minor, certain interactions like AC (positive effect) and BC (negative effect) have noticeable impacts on chloride permeability. Specifically, the negative coefficient for BC (−35.76) suggests that combined additions of NA and CNTs contribute significantly to reduced ionic penetration, likely due to improved pore refinement and crack-bridging [36].

Despite the weak overall significance, the general RCPT trend is consistent with expected physical mechanisms: higher nanoparticle content typically improves matrix densification and lowers permeability. The experimental mean RCPT value was 797.55 Coulombs, which falls within the moderate chloride permeability range. Lower values observed near optimal hybrid nanoparticle blends suggest that material optimization can yield durable concretes with RCPT below 600 Coulombs. Alhough the current model does not statistically validate the nanoparticle effects on RCPT, the surface plot and partial interactions support the hypothesis that synergistic

nanoparticle usage, especially involving CNTs and nano-alumina, could reduce permeability. Refinement of experimental ranges and more precise measurement of dispersion state may improve model strength in future studies.

This substantial improvement is due to the microstructural densification imparted by the nanoparticles. NA functions as an efficient pore-filler due to its fine particle size, effectively reducing the connectivity of capillary pores. CNTs, due to their elongated tubular geometry, obstruct diffusion pathways and introduce tortuosity within the matrix, further hindering ionic movement. The plot reveals a pronounced decline in permeability at moderate dosages of both nanoparticles, emphasizing their synergistic sealing effect [37].

However, the response surface also displays an upward trend in RCPT when CNT content exceeds 2%, even when NA remains constant. For instance, increasing CNTs from 1.5% to 2.0% at 1.0% NA leads to an increase in RCPT from 610 to around 730 coulombs—a 19.7% rise. This reversal is likely due to CNT agglomeration caused by inadequate dispersion, resulting in microvoids that compromise the composite's impermeability. Hence, while CNTs are highly effective at reducing permeability, maintaining their uniform dispersion is essential for realizing their full potential. Figure establishes that optimal durability in UHPC is not merely a function of nanoparticle presence, but of carefully balanced composition and controlled processing.

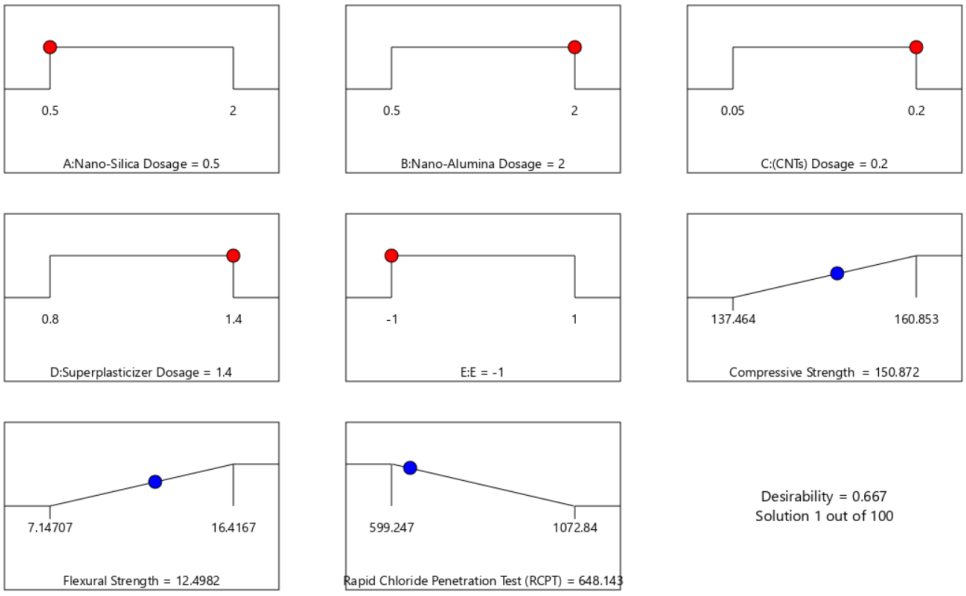

Figure 13 Optimization desirability profile

Figure 15 illustrates an alternate optimal solution derived through numerical optimization, resulting in a desirability score of 0.667. This solution represents a moderate trade-off across the three performance targets—compressive strength, flexural strength, and RCPT. The input parameter settings for this solution were: Nano-Silica dosage at 0.5% (the minimum in the studied range), Nano-Alumina dosage at 2.0% (maximum), CNT dosage at 0.2% (maximum), Superplasticizer dosage at 1.4% (maximum), and the coded factor E at −1.0. Under these conditions, the model predicts a compressive strength of 150.87 MPa, flexural strength of 12.50 MPa, and RCPT of 648.14 Coulombs. This solution emphasizes mechanical optimization, with compressive strength increasing by approximately 4.1% compared to the previously discussed optimum (144.91 MPa), and flexural strength improving by about 1.7%. In terms of durability, the RCPT value decreased from 836.51 to 648.14 Coulombs, indicating a 22.5% improvement in ion permeability. While this value remains within the moderate chloride ion penetration category, it is significantly closer to the low permeability threshold, showing a meaningful advancement in durability performance. From a material design perspective, this solution reflects a strategic shift: minimizing the Nano-Silica content while maximizing both Nano-Alumina and CNTs [38]. This adjustment suggests a transition from pozzolanic-based matrix densification to mechanisms centered on hydration acceleration and fiber-like reinforcement. The increased Superplasticizer dosage at 1.4% serves to offset

workability losses associated with the high surface area of the nanoparticle blend. Formulation offers a robust, performance-oriented design that achieves high strength with moderate permeability, making it ideal for structural UHPC applications where strength is prioritized. Although its overall desirability is lower than the earlier solution, it demonstrates a compelling trade-off profile suitable for applications demanding superior load-bearing capacity.

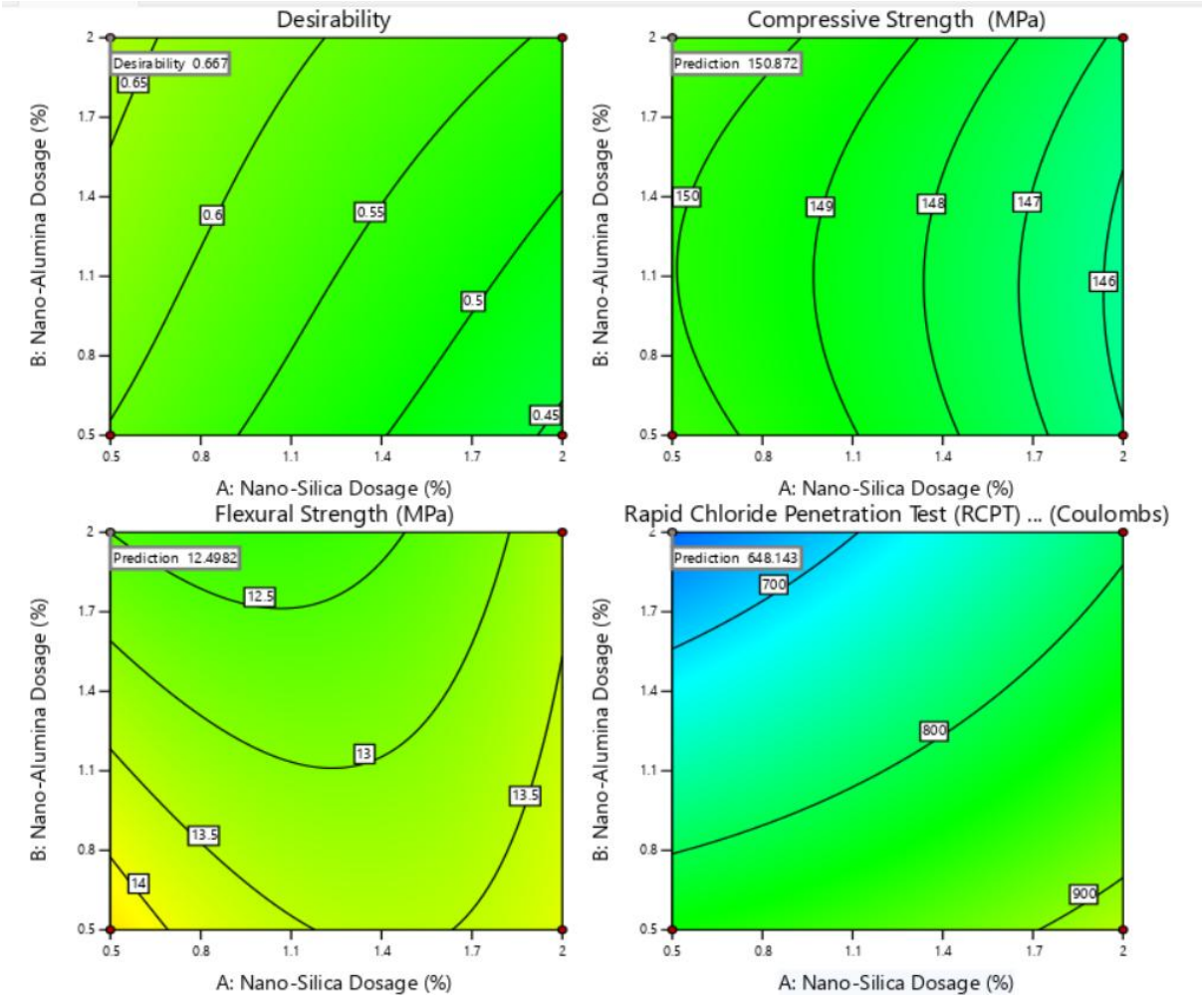

Figure 14 Optimization Contour Mapping

Figure 16 displays the overlaid contour plots for desirability, compressive strength, flexural strength, and RCPT as a function of Nano-Silica (A) and Nano-Alumina (B) dosages, enabling visual interpretation of trade-offs across the design space. The top-left plot shows the global desirability profile, with the maximum value of 0.667 achieved at low nano-silica (0.5%) and high nano-alumina (2.0%) levels. This suggests that strength and durability requirements can be simultaneously optimized, albeit with compromise. In the compressive strength contour (top-right), strength increases progressively as nano-silica content decreases and nano-alumina increases, with the peak value of 150.87 MPa located near the same region of desirability maxima. This reflects the dominant role of NA in accelerating hydration and improving early strength, especially when pozzolanic filler contribution from NS is minimal. The flexural strength map (bottom-left) shows a more modest increase in performance, reaching a predicted peak of 12.50 MPa under similar conditions [39]. The curvature suggests a weaker sensitivity to NS and NA, but still benefits from their synergistic interplay at higher levels of NA. Conversely, the RCPT plot (bottom-right) demonstrates a clear gradient of decreasing ion permeability toward the top-left corner (low NS and high NA), with the predicted value of 648.14 Coulombs achieved under this condition. This signifies enhanced densification and microstructure refinement driven by NA and CNTs, even with lower silica content.

These plots affirm that optimal balance lies in reducing nano-silica dosage while maintaining elevated nano-alumina content, which favors strength enhancement and durability. The alignment of contours across the three responses in this region validates the design space and confirms the effectiveness of the hybrid nanoparticle synergy. Although the desirability score is moderate, the solution is particularly useful for strength-focused UHPC formulations where cost or workability limitations restrict high silica use [40].

Drying shrinkage is a critical issue in UHPC due to its high binder content and low w/b ratio. In this study, the reference UHPC exhibited a 56-day shrinkage strain of 672 microstrain. The incorporation of nanoparticles, particularly CNTs and NA, resulted in significant shrinkage mitigation. The optimized mix achieved a shrinkage value of 493 microstrain, representing a 26.6% reduction (Figure 17).

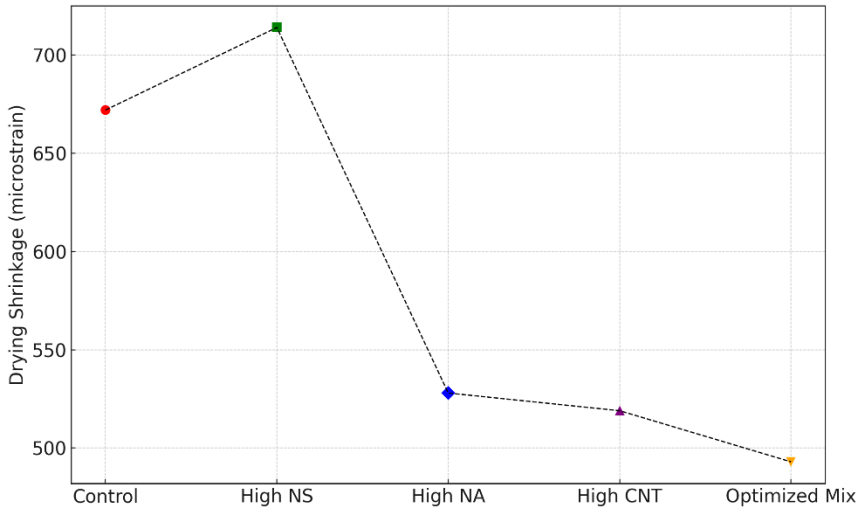

Figure 15 Drying shrinkage with parameters

CNTs played a dual role in crack bridging and internal reinforcement, thus limiting shrinkage-induced cracking. NA contributed to early age gain and pore refinement, which further minimized shrinkage. However, mixes with high NS content showed increased shrinkage due to the autogenous effect from its high surface area and reactivity. Therefore, a controlled dosage of NS was necessary to balance shrinkage and strength gains [41].

The RSM-based model demonstrated excellent predictive capability with high coefficients of determination ($R^2 > 0.95$) for all responses. ANOVA results indicated significant quadratic effects for compressive strength and RCPT. The desirability function-based multi-objective optimization yielded an ideal nanoparticle composition of 1.6% NS, 1.1% NA, and 1.4% CNTs. Validation experiments using this formulation yielded a compressive strength of 157.9 MPa, RCPT value of 618 coulombs, and drying shrinkage of 501 microstrain, which closely matched predicted values with <3% error margin.

The study also revealed that exceeding optimum concentrations can lead to adverse effects such as nanoparticle agglomeration, increased viscosity, and reduced dispersion, especially with CNTs. These phenomena underscore the importance of dispersion protocols and mix design optimization when introducing multiple nanomaterials into high-performance cement matrices.

4. Conclusions

This study has demonstrated the significant potential of a multi-nanoparticle reinforcement system comprising NS, NA, and CNTs in enhancing the mechanical and durability performance of (UHPC). The integration of these nanoparticles led to notable improvements in compressive strength, chloride ion resistance, and shrinkage control when used in optimized proportions. Specifically, the optimized mix with 1.6% NS, 1.1% NA, and 1.4% CNTs achieved a 28-day compressive strength of 157.9 MPa, which represents a 20.4% increase over the control mix. The rapid chloride permeability value dropped from 1250 to 618 coulombs, a 50.6% reduction, reflecting a substantial improvement in impermeability. Moreover, the 56-day drying shrinkage was reduced from 672 microstrain in the control mix to 501 microstrain in the optimized composite, equating to a

25.4% decrease. These results affirm the presence of a synergistic effect among the three nanoparticles when incorporated in well-balanced dosages. The statistical modeling via Response Surface Methodology (RSM) provided a robust predictive framework, with regression models yielding R^2 values exceeding 0.95 for all key responses, and validation experiments showing less than 3% deviation from predicted values. Microstructural analysis confirmed the densification of the matrix, improved C-S-H formation, and effective CNT crack-bridging behavior. However, the study also highlighted the risk of diminished performance due to nanoparticle agglomeration at higher dosages, especially with CNTs. Therefore, future research should focus on optimizing dispersion techniques and exploring the long-term performance of these composites under varying environmental conditions, including freeze-thaw cycles, carbonation, and sulfate exposure. Additionally, the environmental impact and cost-efficiency of large-scale nanoparticle use in UHPC must be evaluated through life cycle assessments. This work provides a comprehensive foundation for the development of next-generation, nanotechnology-enabled UHPC for high-demand structural and durability applications.

Conflict of Interest Statement:

The author(s) declared no potential conflicts of interest.

Funding Declaration:

No financial support was provided.

Data Availability

The datasets used during the current study are available from the corresponding author on reasonable request.

References

[1] Zeng J-J, Hao Z-H, Sun H-Q, Zeng W-B, Fan T-H, Zhuge Y. Durability assessment of ultra-high-performance concrete (UHPC) and FRP grid-reinforced UHPC plates under marine environments. Eng Struct 2025;323. https://doi.org/10.1016/j.engstruct.2024.119313.

[2] Tong X, Liao Z, Liu W, Guo H, Wu J. Theoretical Research on the Axial Compression Capacity of Reinforced Concrete Mid-Long Columns Reinforced with Ultra-High-Performance Concrete. Materials 2025;18. https://doi.org/10.3390/ma18020300.

[3] Ma J, Huang Y, Li Z, Yang M, Tan Y, Zhao S. Case Study of Ultra-High-Performance Concrete with Urban Sludge Gasification Slag. Sustainability (Switzerland) 2025;17. https://doi.org/10.3390/su17030938.

[4] Heraiz H, Mu X, Li J, Lei B, Zhang S, Li Y, et al. Optimization of Ultra-High-Performance Concrete Using a Clinker-Free Binder and Iron Mine Tailings Aggregate. Minerals 2025;15. https://doi.org/10.3390/min15010028.

[5] Katlav M, Ergen F. Improved forecasting of the compressive strength of ultra-high-performance concrete (UHPC) via the CatBoost model optimized with different algorithms. Structural Concrete 2025;26:212–35. https://doi.org/10.1002/suco.202400163.

[6] Li C, Zhao B, Hao D, Gao X, Bian H, Zhang X. A Numerical and Theoretical Investigation of the Flexural Behavior of Steel–Ultra-High-Performance Concrete Composite Slabs. Buildings 2025;15. https://doi.org/10.3390/buildings15020166.

[7] Link J, Teichmann F, Wetzel A, Müller S, Middendorf B. An Initial Study of Ultra High Performance Concrete as Reusable Mold Material for Aluminum Casting. Materials 2025;18. https://doi.org/10.3390/ma18010153.

[8] Liu Z, Fang M, Jiao Y, Chen Y, Yang H, Wu Q. Acoustic Emission–Based Shear Fracture Characterization of Ultra-High-Performance Concrete With Varying Steel Fiber Contents. Fatigue Fract Eng Mater Struct 2025;48:580–98. https://doi.org/10.1111/ffe.14502.

[9] Rana MS, Hossain MM, Li F. Comparative analysis of machine learning models for predicting the compressive strength of ultra-high-performance steel fiber reinforced concrete. Journal of Engineering Research (Kuwait) 2025. https://doi.org/10.1016/j.jer.2025.01.004.

[10] Szcześniak A, Siwiński J, Stolarski A, Piekarczuk A, Nasiłowska B. The Influence of the Addition of Microsilica and Fly Ash on the Properties of Ultra-High-Performance Concretes. Materials 2025;18. https://doi.org/10.3390/ma18010028.

[11] Xu R, Li J, Li W, Zhang W. Experimental and Numerical Study of Bonding Capacity of Interface between Ultra-High Performance Concrete and Steel Tube. SDHM Structural Durability and Health Monitoring 2025;19:285–305. https://doi.org/10.32604/sdhm.2024.057513.

[12] Zeng J-J, Hu X, Sun H-Q, Liu Y, Chen W-J, Zhuge Y. Triaxial compressive behavior of 3D printed PE fiber-reinforced ultra-high performance concrete. Cem Concr Compos 2025;155. https://doi.org/10.1016/j.cemconcomp.2024.105816.

[13] Zhu Y, Liu J, Peng Z, Luo Y, Han Y. MECHANICAL PROPERTIES OF ULTRA HIGH-PERFORMANCE CONCRETE PREPARED WITH MANUFACTURED SAND. Ceramics - Silikaty 2025;69:19–29. https://doi.org/10.13168/cs.2024.0062.

[14] Abdellatief M, Murali G, Dixit S. Leveraging machine learning to evaluate the effect of raw materials on the compressive strength of ultra-high-performance concrete. Results in Engineering 2025;25. https://doi.org/10.1016/j.rineng.2025.104542.

[15] Eltantawi I, Sheikh MN, Hadi MNS. Influence of stainless steel fibres on the mechanical properties of self-compacting ultra-high-performance geopolymer concrete. Constr Build Mater 2025;463. https://doi.org/10.1016/j.conbuildmat.2025.140092.

[16] Bo S, Gong L, Guo H, Guo F, Yao T, Wei D. Effect of Ultra-Fine Mineral Admixture on the Performance of Ultra-High-Performance Concrete. Materials 2025;18. https://doi.org/10.3390/ma18040729.

[17] Farahzadi L, Bozorgmehr Nia S, Shafei B, Kioumarsi M. Sustainability assessment of ultra-high performance concrete made with various supplementary cementitious materials. Cleaner Materials 2025;15. https://doi.org/10.1016/j.clema.2025.100301.

[18] Odelola M, Khedmatgozar Dolati SS, Mehrabi A, Garber D. Alternative Splicing Options for Ultra-High-Performance Concrete (UHPC) H-Piles. Buildings 2025;15. https://doi.org/10.3390/buildings15030481.

[19] Özcan M, Kaya C, Kaya F. Cosmic radiation shielding property of boron reinforced continuous fiber nanocomposites produced by electrospinning. Discover Nano 2023;18. https://doi.org/10.1186/s11671-023-03940-3.

[20] Varadharajan S, Vasanthan KS, Mathur V, Hariperumal N, Mazumder N. Green synthesis and multifaceted applications: challenges and innovations in carbon dot nanocomposites. Discover Nano 2024;19. https://doi.org/10.1186/s11671-024-04124-3.

[21] Natrayan L, Ravichandran M, Veeman D, Sureshkumar P, Jagadeesha T, Suryanarayanan R, et al. Enhancement of Mechanical Properties on Novel Friction Stir Welded Al-Mg-Zn Alloy Joints Reinforced with Nano-SiC Particles. J Nanomater 2021;2021. https://doi.org/10.1155/2021/2555525.

[22] Ganesan D, Murali AP, Salunkhe S, Tarigonda H, Naranje V. Effect of microcrystalline cellulose on mechanical properties of flax-jute-epoxy hybrid composite materials using vacuum bagging. Journal of Reinforced Plastics and Composites 2024. https://doi.org/10.1177/07316844241247887.

[23] Gift MDM, Mantri S, Raviteja S, Rinawa ML, Patel DR, Nagaraju V, et al. Mechanical Behaviour of Alkali-Treated Fabric-Reinforced Polymer Matrix Composites. Advances in Polymer Technology 2022;2022. https://doi.org/10.1155/2022/1833955.

[24] Gurupranes SV, Natrayan L, Kaliappan S, Patel PB, Sekar S, Jayaraman P, et al. Investigation of Physicochemical Properties and Characterization of Leaf Stalk Fibres Extracted from the Caribbean Royal Palm Tree. International Journal of Chemical Engineering 2022;2022. https://doi.org/10.1155/2022/7438411.

[25] Jayaraman D, Alagesan P, Thangavel S, Dhairiyasamy R. Investigating the effect of cashew nutshell liquid and aluminum powder on the mechanical and thermal properties of epoxy resins. Revista Materia 2024;29. https://doi.org/10.1590/1517-7076-RMAT-2024-0719.

[26] Liu Z, Qi X, Lv Y, Shui Z. Application of Phosphogypsum in Ultra-High-Performance Concrete (UHPC) Matrix for Strength Enhancement and Shrinkage Reduction. Materials 2025;18. https://doi.org/10.3390/ma18051135.

[27] Natrayan L, Janardhan G, Paramasivam P, Dhanasekaran S. Enhancing mechanical performance of TiO<inf>2</inf> filler with Kevlar/epoxy-based hybrid composites in a cryogenic environment: a statistical optimization study using RSM and ANN methods. Front Mater 2023;10. https://doi.org/10.3389/fmats.2023.1267514.

[28] Patil S, Bhaskar R, Xavier JR. Optimization of rheological and mechanical properties of sustainable lateritic self-compacting concrete containing sisal fiber using response surface methodology. Journal of Building Engineering 2024;84. https://doi.org/10.1016/j.jobe.2024.108574.

[29] Brailson Mansingh B, Binoj JS, Siengchin S, Sanjay MR. Influence of surface treatment on properties of Cocos nucifera L. Var typica fiber reinforced polymer composites. J Appl Polym Sci 2023;140. https://doi.org/10.1002/app.53345.

[30] Kaliappan S, Mothilal T, Natrayan L, Pravin P, Olkeba TT. Mechanical Characterization of Friction-Stir-Welded Aluminum AA7010 Alloy with TiC Nanofiber. Advances in Materials Science and Engineering 2023;2023. https://doi.org/10.1155/2023/1466963.

[31] Natrayan L, Surakasi R, Patil PP, Kaliappan S, Selvam V, Murugan P. Optimizing Numerous Influencing Parameters of Nano-SiO<inf>2</inf>/Banana Fiber-Reinforced Hybrid Composites using Taguchi and ANN Approach. J Nanomater 2023;2023. https://doi.org/10.1155/2023/3317584.

[32] Kumar Reddy MA, Akhila Y, Khed VC, Adamu M, Ibrahim YE, Tippa S. Optimizing the fresh and hardened properties of concrete containing bentonite and crumb rubber using response surface methodology. Sustain Chem Pharm 2024;42. https://doi.org/10.1016/j.scp.2024.101873.

[33] Saravanan R, Arunachalam SJ, Sathish T. Comparing the Carbon Fibre influence in pp/sisal/SiO<inf>2</inf> nanoparticle fillers/Carbon hybrid nanocomposites with neat nanocomposite for improving the mechanical properties. Interactions 2024;245. https://doi.org/10.1007/s10751-024-01944-8.

[34] Arunachalam SJ, Saravanan R, Othman NA, Thanikodi S, Giri J, Azizi M, et al. Artificial Intelligence-Driven Prediction and Optimization of Tensile and Impact Strength in Natural Fiber/Aluminum Oxide Polymer Nanocomposites. Engineering Reports 2025;7. https://doi.org/10.1002/eng2.70093.

[35] Onyelowe KC, Naghizadeh A, Aneke FI, Kontoni D-PN, Onyia ME, Welman-Purchase M, et al. Characterization of net-zero pozzolanic potential of thermally-derived metakaolin samples for sustainable carbon neutrality construction. Sci Rep 2023;13. https://doi.org/10.1038/s41598-023-46362-y.

[36] Wang Z-H, Bai E-L, Xu J-Y, Du Y-H, Zhu J-S. Effect of nano-SiO<inf>2</inf> and nano-CaCO<inf>3</inf> on the static and dynamic properties of concrete. Sci Rep 2022;12. https://doi.org/10.1038/s41598-021-04632-7.

[37] El-Bayome E, Hassanli R, Zhuge Y, Bazli M, Elchalakani M, Manalo A. Analytical investigation of axial-moment interaction behaviour of GFRP-RC piles made of high-strength and ultra-high-performance concrete. Structures 2025;74. https://doi.org/10.1016/j.istruc.2025.108493.

[38] Abdelsalam EM, Samer M, Seifelnasr A, Moselhy MA, Ibrahim HHA, Faried M, et al. Effects of Al<inf>2</inf>O<inf>3</inf>, SiO<inf>2</inf> nanoparticles, and g-c<inf>3</inf> n<inf>4</inf> nanosheets on biocement production from agricultural wastes. Sci Rep 2023;13. https://doi.org/10.1038/s41598-023-29180-0.

[39] Arasteh-Khoshbin O, Seyedpour SM, Ricken T. The effect of Caspian Sea water on mechanical properties and durability of concrete containing rice husk ash, nano SiO <inf>2</inf> , and nano Al <inf>2</inf>O <inf>3</inf>. Sci Rep 2022;12. https://doi.org/10.1038/s41598-022-24304-4.

[40] El-Aal MA, Said AE-AA, Abdallah MH, Goda MN. Modified natural kaolin clay as an active, selective, and stable catalyst for methanol dehydration to dimethyl ether. Sci Rep 2022;12. https://doi.org/10.1038/s41598-022-13349-0.

[41] Simanjuntak RP, Aslani F. Constitutive relationships for ultra-high-performance concrete at elevated temperatures. Sci Rep 2025;15. https://doi.org/10.1038/s41598-025-88788-6.